Nutrient exchange and ventilation of benthic gases across the continental shelf break

S. A. Siedlecki,[1] D. E. Archer,[1] and A. Mahadevan[2]

[1]   On western margins of ocean basins, such as the eastern continental shelf of the United States, rates of biological productivity are higher than in the open ocean, in spite of the mean downwelling circulation. We use a nonhydrostatic, three-dimensional, process study ocean model with idealized shelf-slope geometry, wind forcing, and tracers to explore the interplay between the circulation and the biogeochemistry of the shelf and slope; the pathways that can transport nutrients from the deep ocean and from the sediments to the surface ocean euphotic zone. Cross-shelf exchange between the open and coastal ocean is regulated by a shelf break front that separates light waters on the shelf from denser waters on the slope. The wind direction and strength influence both the position and slope of the isopycnals at the front, which become more vertical in response to northerly winds and flatten in response to southerly winds. When the wind direction oscillates between northerly and southerly, it pumps nutrient and gas-rich bottom boundary layer water up to the sea surface. Nutrients tend to accumulate in the benthic boundary layer during southerly winds and are pumped to the surface during periods of northerly winds. Stratification of the water column in summertime reduces the shelf break pump by dampening the effect of the winds on the movement of the front. When extrapolated over the northeast coast of the United States, the nutrients supplied by the shelf break pump from the open ocean to the coastal ocean are three times the estimated nitrogen delivered to the shelf from estuaries.

1.   Introduction

[2]   The coastal ocean comprises 18–33% of the entire ocean's biological production despite covering only 8% of the global ocean area [*Wollast*, 1991]. With the exception of a few areas influenced by the world's largest rivers, coastal ocean productivity is maintained by nutrients supplied from the deep open ocean.

[3]   The coastal ocean and open ocean are typically separated by lateral density gradients or fronts, which can be differentiated along continental shelves using the classification system from *Hill et al.* [1998] and *Loder et al.* [1998a], and are compiled in Figure 1. Thermohaline or shelf break fronts, which will be the focus in this study, are shown by red areas in Figure 1 and separate light, fresh, shelf waters from denser slope waters.

[4]   Coastal circulation is not well resolved in global-scale carbon cycle models, and so the role of the coastal ocean is not well quantified. Two mechanisms have been described which might bring nutrients into the euphotic zone in regimes dominated by shelf break fronts, on the western ocean margins, characterized by wide continental shelves (e.g., off the east coast of the United States): shelf break upwelling and bottom boundary layer detachment. Shelf break upwelling differs from wind-driven upwelling in that nutrients are brought to the surface along isopycnals comprising the front as the jet associated with the front meanders across the shelf break due to baroclinic instability. Meanders in the front draw slope water up and onto the shelf. *Atkinson et al.* [1984] observed a large nutrient flux onto the southeastern U.S. continental shelf from shelf break upwelling in the summertime and concluded that this is the most significant source of nitrate to the shelf waters. *Campos et al.* [2000] described the interaction of shelf break upwelling and the meandering Brazil Current and winds in the Southeast Brazil Bight. *Castelao et al.* [2004] modeled the interaction of the Brazil Current with the winds and the associated shelf break upwelling. During the winter, water was primarily upwelled as a result of the meanders, and during the summer, the upwelling was primarily due to the wind direction. In all these studies, this mechanism was observed to onwell water onto the shelf from much deeper than 200m, bringing nutrients to the surface. This could potentially also ventilate high-pCO_2 waters of the thermocline.

[5]   Bottom boundary layer convergence and detachment serves as a second potential mechanism for benthic ven-

[1]Department of Geophysical Sciences, University of Chicago, Chicago, Illinois, USA.
[2]Department of Earth Sciences, Boston University, Boston, Massachusetts, USA.
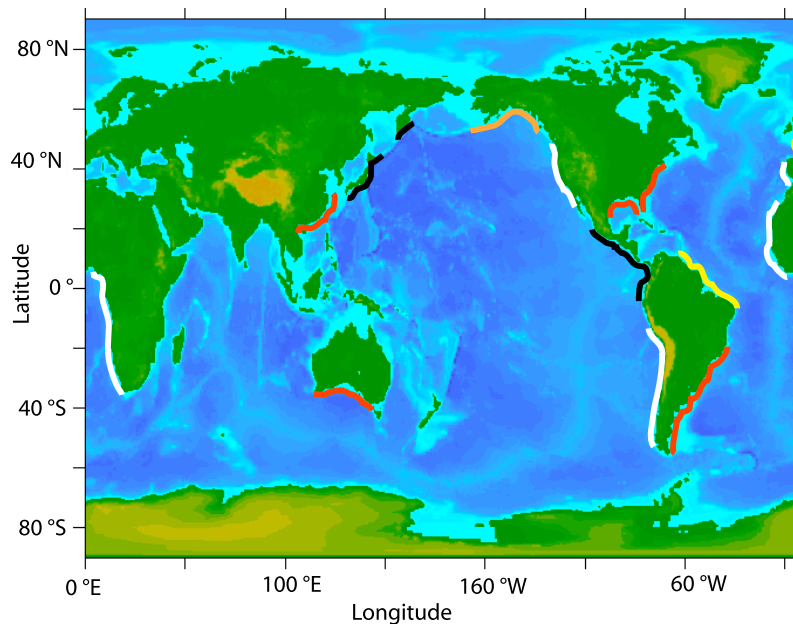
Figure 1. Map showing the prevalence of fronts in coastal regions. Each colored region designates a different type of front on the basis of observations and regional synthesis by *Hill et al.* [1998] and *Loder et al.* [1998a]. Global bathymetry data are from ETOPO5. Yellow areas outline regions with plume fronts. Black areas outline areas with equatorial or polar fronts. Orange areas outline regions with tidal mixing fronts. Red areas outline regions with shelf break fronts consistent with the one modeled in this study.

tilation and nutrient supply to the euphotic zone at the shelf break. *Gawarkiewicz and Chapman* [1992] identified a detachment of the bottom boundary layer, extending offshore along the isopycnal surface, and carrying neutrally buoyant particles with it. Their three-dimensional frontogenic modeling study focused on the buoyancy driven part of the flow, neglecting wind forcing. In an idealized model for the east coast of the United States, *Chapman and Lentz* [1994] found that the position of the front is stabilized by a convergence in the bottom boundary layer. Such convergence upwells water from the bottom boundary layer around the foot of the front, potentially bringing nutrient rich waters from the bottom boundary layer to the surface.

[6] Both bottom boundary layer detachment and convergence have been the subject of many observational studies. In an experiment by *Houghton and Visbeck* [1998], dye was injected into the bottom boundary layer water and observed later upwelled along the isopycnals of the front. *Lozier and Gawarkiewicz* [2001] measured cross-shelf exchange using drifters and found it occurred everywhere along the front, independent of local bathymetric features. Drifters released at 10 m and 40 m were detrained into the shelf break current and the majority was ejected at the surface at the front. Using a simple advective-diffusive model and synoptic cross sections of the Mid-Atlantic Bight frontal jet, *Pickart* [2000] suggested that convergence within the bottom boundary layer is what drives the detachment. *Linder et al.* [2004] pointed out that the detached layer is capable of intruding into the euphotic zone in the winter and spring. *Hales et al.* [2009a, 2009b], observed a particle plume originating from the bottom boundary layer, carrying boundary layer chemistry, and

fueling a phytoplankton maximum at the shelf break front. In addition to nutrients, high concentrations of methane have been found in the bottom boundary layer off the east coast in the Mid-Atlantic Bight [*Newman et al.*, 2008]. *DeGrandpre et al.* [2002] measured high carbon dioxide concentrations at the outer shelf of the South Atlantic Bight in the summer, consistent with deep ocean interior water upwelled to the sea surface along the front.

[7] In this study, we use a three-dimensional numerical model adapted from an existing model for open ocean fronts [*Mahadevan et al.*, 1996a, 1996b; *Mahadevan and Archer*, 2000; *Mahadevan*, 2006] to examine the pathways for nutrient supply into the euphotic zone, from the deep ocean interior and from the sediment surface, in a thermohaline frontal regime. We use idealized tracers to quantify the geochemical fluxes, of nutrients flowing into the euphotic zone, and benthic methane exposure to the atmosphere at the sea surface. We use the model to predict the response of the geochemical pathways to environmental conditions such as water column stratification, which varies seasonally, and wind strength and direction.

2. General Circulation of the Mid-Atlantic Bight

[8] The Mid-Atlantic Bight region is characterized by a semipermanent thermohaline front at the shelf break separating the fresh shelf waters from the more saline waters of the slope sea (SEEP-I, SEEP-II) [*Walsh et al.*, 1988; *Aikman et al.*, 1988; *Biscaye et al.*, 1994; *Shaw et al.*, 1994]. The position of the foot of the front on the seafloor is usually between 60 and 120 m deep, with a climatological
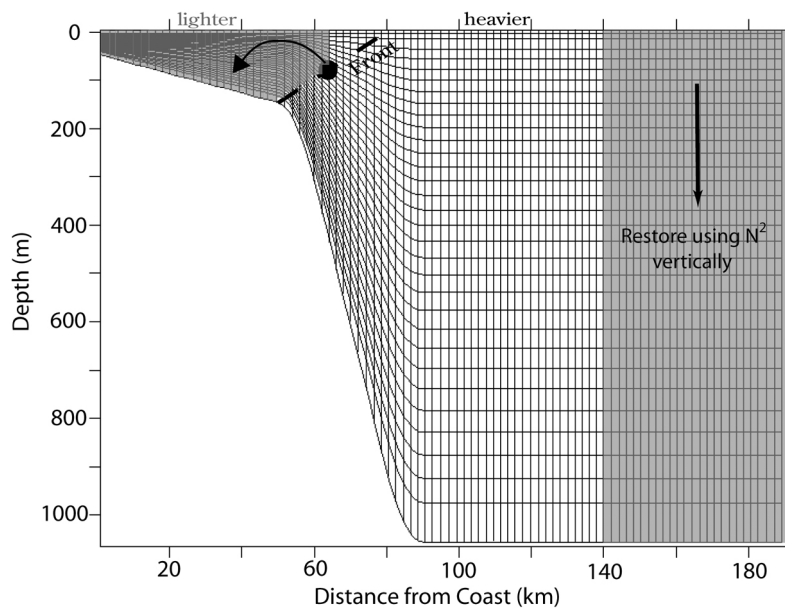
Figure 2. A slice of the model sigma grid and topography used to define the model domain. Shaded areas depict regions of the grid where restoration of the density profile occurs. Near the offshore boundary the density profile is restored to the alongshore-averaged density profile with a time scale of 1 day. On the shelf, to simulate freshening from rivers, the density profile is restored to the initial value with a time scale of 60 days. This is achieved by locating the isopycnal of the front midwater column and by restoring the water column that is lighter than that isopycnal. See the text for further explanation.

average of 75 m [*Rasmussen et al.*, 2005]. Although the front meanders up to 50 km horizontally on short time scales, it is usually found within a narrow band (10–20 km), extending hundreds of km, following the shelf break [*Loder et al.*, 1998b; *Fratantoni and Pickart*, 2007].

[9] The density difference of waters across the front is largely a function of salinity, driven by fresh waters flowing from the north in the Labrador Current [*Loder et al.*, 1998b]. The front persists throughout the year, despite the summer-time thermal stratification of waters on the shelf. The flux of shelf water with a salinity less than 34.8 from the north is estimated to be 0.38 Sv while the flux across the front, or export of shelf water to the open ocean over 800 km of shelf, is roughly estimated to be 0.35 Sv [*Loder et al.*, 1998b].

[10] The front is associated with a horizontal density difference between the lighter shelf waters and denser slope waters of about 0.3 kg m^{-3}. The density contrast generates a jet in the same direction as the mean flow to the south. The core velocity ranges from about 0.2 m s^{-1} in the winter to 0.3 m s^{-1} in the summer [*Linder and Gawarkiewicz*, 1998]. The mean jet found between the 125–150 m isobaths is 15–25 km wide and has a mean depth of 50 m [*Linder and Gawarkiewicz*, 1998].

[11] Mean offshore currents (~0.01 m s^{-1}) exist on the shelf and become stronger with depth and distance from shore [*Biscaye et al.*, 1994]. These offshore currents in the bottom boundary layer are thought to help stabilize the mean frontal position over hundreds of km of the shelf [*Chapman and Lentz*, 1994; *Chapman*, 2000]. Studies that have explored the mechanisms for export of shelf water to the open ocean have focused on the surface ocean, specifically Gulf Stream

rings and frontal instabilities [*Mitzoba et al.*, 2006; *Okkonen et al.*, 2003; *Ryan et al.*, 1999].

3. Model Description

3.1. Physical Model

[12] Our three-dimensional model, PSOM, is a non-hydrostatic, high-resolution (horizontal grid spacing of 2km) model of an oceanic front [*Mahadevan et al.*, 1996a, 1996b; *Mahadevan*, 2006; *Mahadevan and Archer*, 2000] that was modified for use in the coastal setting. The model is configured to an idealized geometry of the Mid-Atlantic Bight of the United States after *Gawarkiewicz and Chapman* [1992]. The domain extends 48 km in the alongshore direction, or about twice the internal Rossby radius on the slope and nearly 10 times the internal Rossby radius on the outer shelf, and 192 km in the offshore direction. The depth ranges from 40 m on the shelf to 200 m at the shelf break situated 55 km offshore of the shoreward boundary, to 1000 m on the slope. A stretched sigma grid with 32 levels gives higher vertical resolution on the shelf than offshore, as shown in Figure 2. The vertical resolution ranges from <2 m on the shelf to more than 30 m offshore. In order to resolve the bottom boundary layer and surface Ekman flow, the bottom and top layer of grid cells are held at a uniform thickness of 8 and 5 m, respectively. The north and south boundaries are periodic. The shoreward, offshore, and bottom boundaries are closed.

[13] The General Ocean Turbulence Model (GOTM) using the Mellor-Yamada 2.5 turbulence closure scheme [*Mellor and Yamada*, 1982] determines vertical mixing in the model. However, the model does not include tides and waves that

Table 1. Summary of All Model Experiments Indicating Wind Forcing, Averaged Velocities, and Biological Production Within the Front[a]

Case	Wind Stress (N m^{-2})	Wind Period (days)	Stratification	Surface V (m s^{-1})	Bottom V (m s^{-1})	Within the Front: Alongshore-Averaged Production (g C m^{-2} yr^{-1})	U (m s^{-1})
Real winds	0.15	NA[b]	winter	0.027	−0.011	175.4	0.02 +/− 0.2
Real winds summer	0.15	NA	half summer	0.031	−0.010	3.10	0.09 +/− 0.09
Real wind summer full	0.15	NA	summer	0.033	−0.009	54.93	0.14 +/−0.3
No winds	0	0	winter	−0.0004	0.0004	11.82	0.04 +/− 0.02

Case	Wind Stress (N m^{-2})	Wind Period (days)	Stratification	Surface V (m s^{-1}) Southerly	Surface V (m s^{-1}) Northerly	Bottom V (m s^{-1}) Southerly	Bottom V (m s^{-1}) Northerly	Within the Front: Alongshore-Averaged Production (g C m^{-2} yr^{-1}) Southerly	Production Northerly	U (m s^{-1}) Southerly	U (m s^{-1}) Northerly
Oscillating wind	0.05	10	winter	0.059	−0.061	−0.050	0.043	34.92	52.70	−0.040	0.1
Oscillating wind summer	0.05	10	summer	0.001	0.007	−0.021	0.012	43.25	21.38	0.03	0.16
Oscillating wind summer 2	0.05	10	half summer	0.0009	0.008	−0.020	0.010	31.99	13.17	0.020	0.150
Oscillating wind summer 3	0.05	10	0.75 summer	0.001	0.008	−0.020	0.009	45.14	15.93	0.010	0.15
Oscillating wind magnitude 1	0.02	10	winter	0.002	0.0002	−0.014	0.011	16.65	19.39	−0.01	0.04
Oscillating wind magnitude 2	0.1	10	winter	0.012	−0.0002	−0.076	0.054	71.59	144.0	−0.120	0.17
Oscillating wind magnitude 3	0.15	10	winter	0.018	0.0009	−0.115	0.083	142.90	179.5	−0.21	0.24
Oscillating wind period 2	0.05	2	winter	0.0006	0.0008	0.0003	0.0008	35.37	34.98	0.04	0.04
Oscillating wind period 3	0.05	5	winter	0.004	−0.00007	−0.001	0.0005	38.27	38.56	0.030	0.03
Oscillating wind period 4	0.05	15	winter	0.021	−0.064	−0.042	0.045	36.23	72.59	−0.07	0.12

[a]V is the across-shelf velocity, while U is the alongshore velocity. For the case of oscillatory wind forcing, averages over times of northerly or southerly wind stress are calculated. For all other cases, a time average was calculated. The area within the front is defined by 40–60 km offshore.
[b]NA, not applicable.

can generate mixing in the real ocean. Diffusivities for momentum and tracers are assumed to be the same. Further details of the model can be found in Appendix A.

[14] The model is initialized with a horizontal density difference of 0.3 kg m^{-3} at the shelf break, in agreement with observations from the Mid-Atlantic Bight. The shelf water is less dense than the slope water and, to retain the horizontal density difference over time, the shelf water is restored to a reference density with a specified time scale (τ_{shelf}) using:

$$\frac{D\rho}{Dt} = \frac{-(\rho - \rho_{shelf})}{\tau_{shelf}} \qquad (1)$$

where ρ is potential density, ρ_{shelf} is the reference density or the initialized density profile on the shelf, and τ_{shelf} is 60 days for winter and 1 day for summer. Here, and in all following equations, D/Dt refers to the material derivative operator and includes the effect of advection by the fluid in three dimensions. The area to be restored is determined by, first, locating the surface point associated with the mid-water position of the initialized isopycnal which defines the front, as shown in Figure 2. Then, the lighter shelf water is restored to its initialized value according to equation (1) over the whole water column on the shelf.

[15] In steady state, the fresh water flux equivalent to the salinity restoring scheme must balance the fresh water equivalent to the fluid exchange across the front. While the exchange of water across the front is difficult to quantify, the total density-weighted volume flux of restored water divided by the horizontal density gradient in the model (0.3 kg m^{-3}) generates an exchange flux. The exchange flux per unit

distance along the shelf ranges from 0.2 m^2 s^{-1} without winds in the winter to 0.4 m^2 s^{-1} with the realistic wind forcing in the winter, and 1.2 m^2 s^{-1} in the summer. *Loder et al.* [1998b] estimate the annual mean net shelf-ocean volume transport per unit along-shelf distance for the Mid-Atlantic Bight to be 0.44 m^2 s^{-1}, with an implied mean salinity of 33.3 for the transported water. While the summer exchange flux is higher than observed for the Mid-Atlantic Bight, the modeled exchange falls within the observed range of 0.1–4.3 m^2 s^{-1} reported along the east coast of the United States [*Loder et al.*, 1998b].

[16] Along the offshore wall, the density is also restored to dampen upwelling associated with the closed boundary:

$$\frac{D\rho}{Dt} = \frac{-(\rho_{avg} - \rho_{slope})}{\tau_{slope}} \qquad (2)$$

where ρ_{slope} is the initialized density profile at the offshore wall, and τ_{slope} is the restoring time scale of 1 day. The restoring is done over the entire water column within 30 km of the offshore boundary. The term ρ_{avg} is the alongshore-averaged density field in the model; such restoring does not obliterate along-front variability [*Lathuilière et al.*, 2010].

3.2. Numerical Experiments

[17] Three different wind regimes are used to force the model as described in Table 1: no wind, an oscillating wind, and winds from NRDC buoy data. The mean circulation from the no-wind control case is shown in Figure 4. In the oscillating wind case, the wind oscillates sinusoidally in time between southerly, which is against the direction of the geostrophic flow at the front, or up front, and northerly,
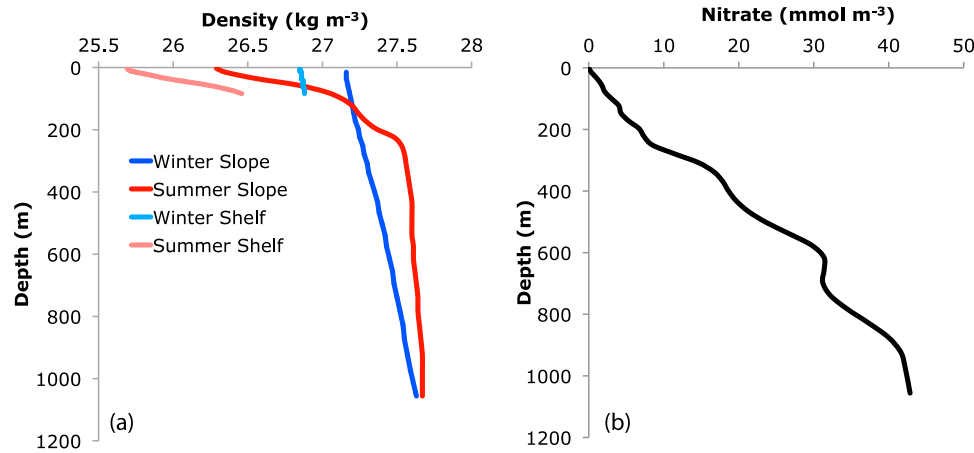
Figure 3. (a) Initialization of winter and summer density structure for both the shelf and the slope. The shelf and slope are separated by a shelf break front with a horizontal density gradient of 0.3 kg m^{-3}. (b) Initial nitrate profile from *Pelegrí and Csanady* [1991].

or down front. Model experiments were run with wind periods of 2, 5, 10, and 15 days, and a wind stress magnitude range that falls within the bounds set by the buoy wind data (+/−0.05–0.15 N m^{-2}). The realistic wind forcing uses 1 year of data from a buoy located in the North Atlantic.

[18] Two seasons are modeled: winter and summer. Each is maintained perpetually for 350 days to allow the model physics and tracers to evolve to a quasi–steady state. The initialization of each season is based on data from the SEEP-I study [*Biscaye et al.*, 1994] and is shown in Figure 3. The horizontal density gradient is the same for both seasons, but the vertical stratification differs. The shelf waters are essentially unstratified in the winter while they are strongly stratified in the summer. In order to evaluate the effect of stratification on the nutrient fluxes, model experiments are run where the summer stratification is weakened by a factor of 2.

3.3. Tracers

[19] Three different kinds of tracers are used in the model: a nitrate-like tracer, bottom boundary layer tracers, and a methane-like tracer. Nitrate is a phytoplankton nutrient, with a deep water source, which fuels what is called "new" production (as opposed to recycled production fueled by ammonia). The nitrate-like tracer is initialized with an open ocean profile of nitrate, $N_0(z)$, from *Pelegrí and Csanady* [1991] (Figure 3). When the nutrient concentration, N, in the euphotic zone is higher than the initialized value N_0 (i.e., $N > N_0$), the excess N decays with time to N_0 following first-order kinetics. The rate of N uptake is recorded as biological uptake. When the nutrient concentration is less than the initialized profile at depth (i.e., $N < N_0$), N grows toward N_0 to simulate the redissolution, or remineralization, of the sinking organic matter:

$$\frac{DN}{Dt} = \frac{\partial}{\partial z}\left(\kappa \frac{\partial N}{\partial z}\right)$$

$$+ \begin{cases} -(N - N_0)\lambda_{prod}e^{-\frac{z}{z_0}} & if (N > N_0) \quad for \quad z < 100m \\ -(N - N_0)\lambda_{remin} & if (N < N_0) \quad for \quad for \quad all \quad z \end{cases}$$

$$(3)$$

where N is the concentration of nutrient in mmol m^{-3}, N_0 (z) is the initial concentration of the nutrient tracer shown in Figure 3, λ_{prod} is an *e*-folding rate of uptake of 0.17 d^{-1}, λ_{remin} is the remineralization rate and is set equal to λ_{prod}, z_0 is 30 m, z is depth in m, and κ is vertical diffusivity for the tracers which has an equivalent value to the vertical viscosity (K_z). The uptake rate is consistent with observations [*Elskens et al.*, 1997; *Harrison et al.*, 1996]. Attenuation of light in the euphotic zone is represented by exponential decay, and assymptotes to zero at 100 m. The consumption of the tracer (i.e., new production) is used to determine the flux of nutrients on to the shelf as a function of wind direction, wind magnitude, and stratification.

[20] Bottom boundary layer tracers were designed to determine the source of the upwelled waters. The boundary layers of the shelf and slope are distinguished by two independent tracers, which are restored to their initialized distribution (B_0) of 1 within 10 m of the bottom using:

$$\frac{DB}{Dt} = \frac{\partial}{\partial z}\left(\kappa \frac{\partial B}{\partial z}\right) - (B(z = z_{bot}) - B_0)\lambda_{degas},$$

$$where \quad \kappa \frac{\partial B}{\partial z}\bigg|_{z=0} = w_{gas}B(z = 0)$$

$$(4)$$

where $B(z = z_{bot})$ is the concentration of bottom boundary layer tracer in mmol m^{-3} at the bottom, λ_{degas} is the decay rate (0.58 d^{-1}), B_0 is the initial concentration at the bottom, and $B(z = 0)$ is the concentration of bottom boundary layer tracer at the surface. The bottom boundary layer tracers are lost when they reach the surface at a rate like that of outgassing by a piston velocity w_{gas} = 3 m d^{-1}.

[21] The methane-like tracer is used to investigate ventilation of the shelf and slope by shelf break upwelling as a function of wind direction, wind magnitude, and stratification.

$$\frac{DCH_4}{Dt} = \frac{\partial}{\partial z}\left(\kappa \frac{\partial CH_4}{\partial z}\right) - CH_4\lambda_{oxid},$$

$$where \quad \kappa \frac{\partial CH_4}{\partial z} = \begin{cases} w_{gas}CH_4 & at \ z = 0 \\ M_{vent} & at \ z = z_b \end{cases}$$
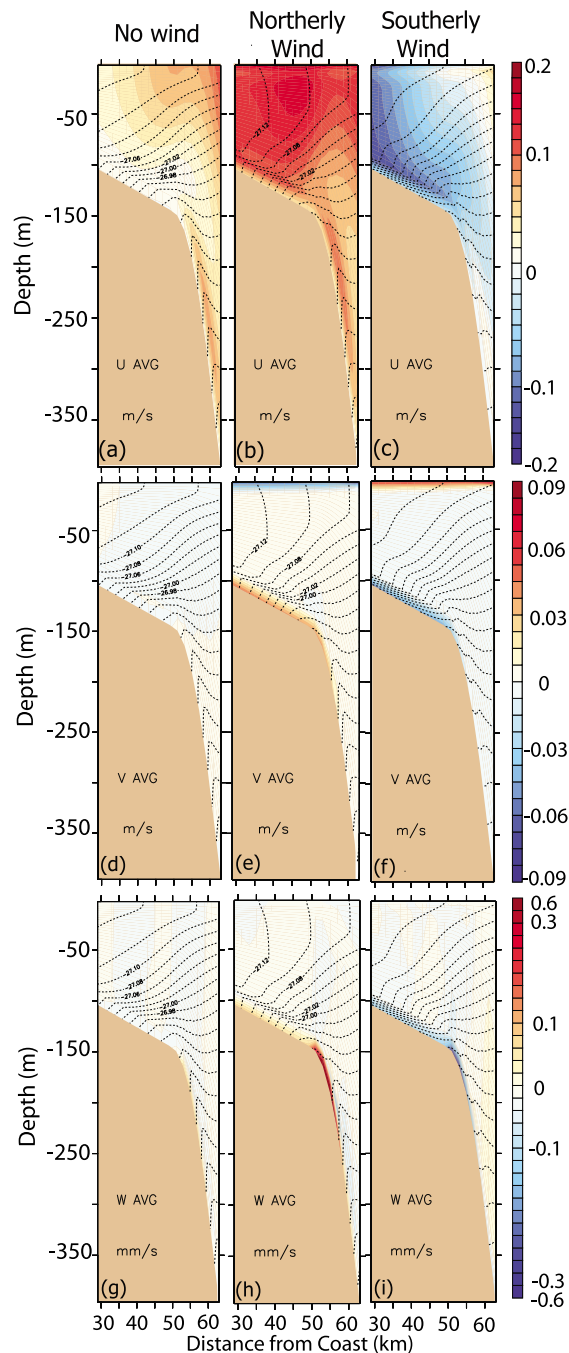
$$(5)$$

Figure 4. Time-averaged velocities along a cross-shelf section shown for the winter case. (a–c) The alongshore u velocity in m s^{-1}. (d–f) The cross-shelf v velocity in m s^{-1}. (g–i) The vertical velocity on the shelf in mm s^{-1}. The positive direction of the velocities is down front (toward the south) for the u velocity, offshore (eastward) for the v velocity, and up for the w velocity. Contours represent averaged density. Figures 4a, 4d, and 4g show the circulation without winds, averaged over the entire period, after initial equilibration. Figures 4b, 4e, and 4h and Figures 4c, 4f, and 4i show the case forced with an oscillating wind of period 10 days and averaged over periods of down-front (from the north) and up-front (from the south) wind stress, respectively, after an initial equilibration period. The color scale for w is not linear.

where CH_4 is the concentration of methane in units of mol CH_4 m^{-3}, λ_{oxid}, the rate at which methane oxidizes in the water column, is 0.033 d^{-1}, which is equivalent to a turnover rate of 30 days. At the surface, z = 0, CH_4 degasses with a piston velocity w_{gas} = 3 m d^{-1}. The constant piston velocity neglects the effect of wind speed on exchange velocity, but this simplification is minor in the context of the larger issue of getting the methane from the benthic boundary layer to the ocean surface. The flux of methane from the sediments is prescribed as $M_{vent} = 1.2 \dfrac{z}{D_{slope}}$, where D_{slope} is the total depth of the model domain (1050 m), and 1.2 mol CH_4m^{-2} d^{-1} or 28 g CH_4m^{-2} yr^{-1} is the observed flux of methane from the sediments on the slope; that is, at z = D_{slope} [*Reeburgh*, 2007]. Methane is released from the sediments uniformly, which is consistent with measurements of methane in the bottom boundary layer that indicate it is uniformly distributed over the shelf [*Newman et al.*, 2008].

[22] The oxidation rate constant for methane in the model is faster than an observed methane lifetime of 1.5 years in a coastal ocean with active venting [*Valentine et al.*, 2001]. By shortening the oxidation lifetime, the methane concentration in the model is able to come into steady state within a computationally feasible time frame. However, as a consequence of the rapid turnover rate in the model, more methane is oxidized in the water column of the model than would be in the real ocean, and therefore the fraction of the degassing flux that reaches the atmosphere in the model is conservative: if anything, underestimated.

4. Results

4.1. Comparison of Model Physics With Observations

[23] A key feature of shelf break front dynamics is the response of the bottom boundary layer to the winds and the alongshore flow. Ekman theory dictates that a northerly (down front) wind will drive an onshore flow at the sea surface. The alongshore current flowing to the south on the shelf is frictionally retarded near the seafloor and generates an offshore cross-isobath flow in the bottom boundary. The opposite circulation develops in response to southerly or up-front winds. These circulation patterns can be seen in averages of flow field snapshots from northerly or southerly wind events in the model (see Figures 4 and 5), from the period after 120 days, once the model has reached a quasi-equilibrated state.

[24] The shelf break jet reaches between 80 and 120 m depth, and the core of the frontal jet is in the upper 50 m of water (Figures 4a–4c for the winter and Figures 5a and 5b for the summer). The modeled maximum and average jet velocities for summer, winter, up-front and down-front wind forcings are reported in Table 1. The average seasonal jet velocities are consistent with observations: the winter jet is slower than the summer jet.

[25] After a spin-up time of about 100 days, a second jet develops on the slope, deeper and stronger than the shelf break jet. The average modeled velocity of the slope jet is 0.3 m s^{-1} in the winter and 0.6 m s^{-1} in the summer, and its influence extends as deep as 800 m (Figure 6). In observations, the slope jet is weaker than the shelf break jet, and weaker than the slope jet in the model. This discrepancy
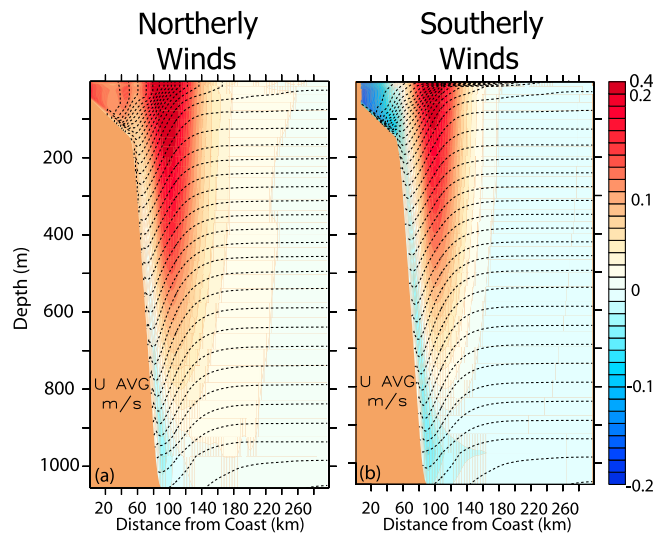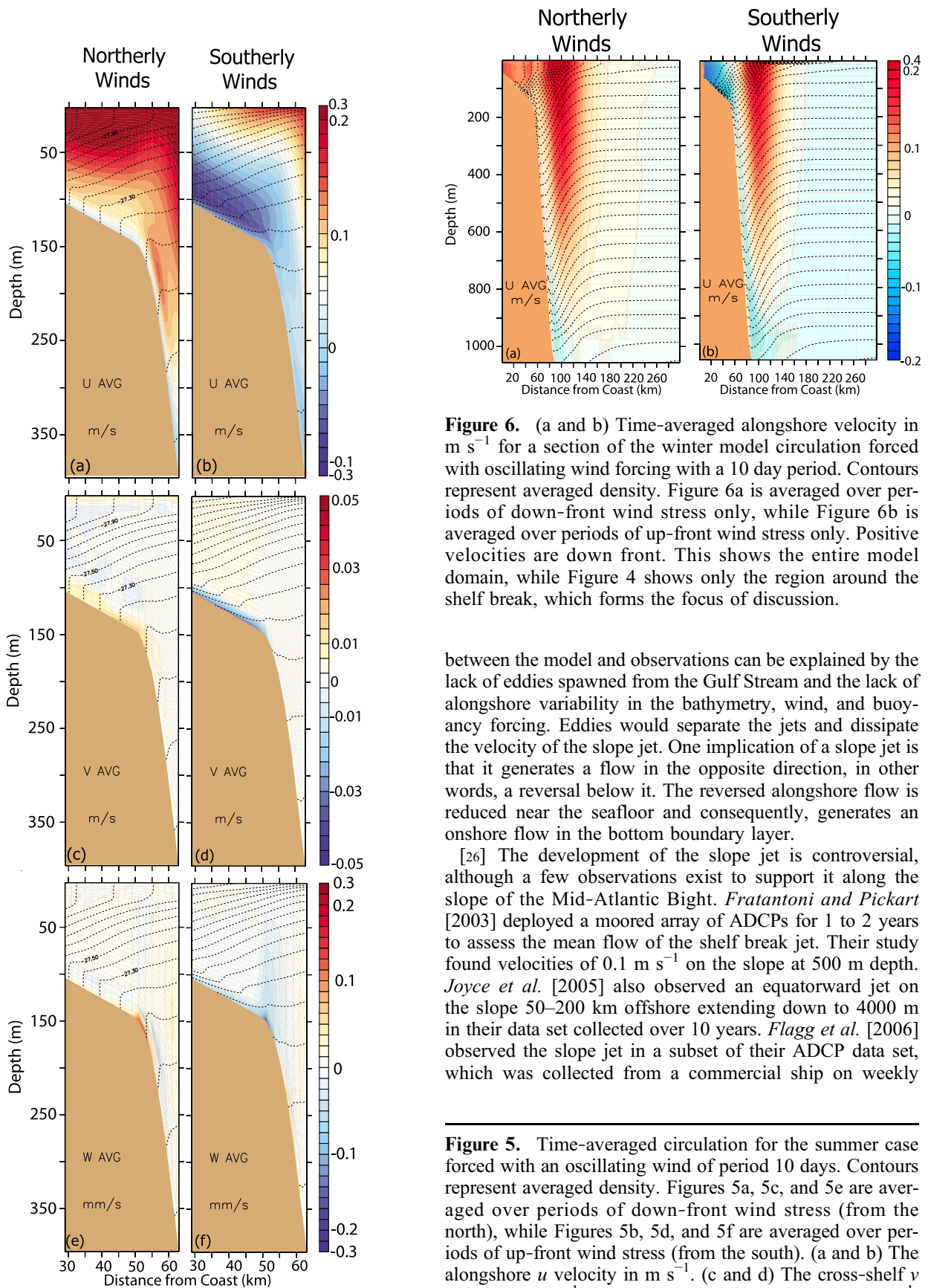
Figure 6. (a and b) Time-averaged alongshore velocity in m s^{-1} for a section of the winter model circulation forced with oscillating wind forcing with a 10 day period. Contours represent averaged density. Figure 6a is averaged over periods of down-front wind stress only, while Figure 6b is averaged over periods of up-front wind stress only. Positive velocities are down front. This shows the entire model domain, while Figure 4 shows only the region around the shelf break, which forms the focus of discussion.

between the model and observations can be explained by the lack of eddies spawned from the Gulf Stream and the lack of alongshore variability in the bathymetry, wind, and buoyancy forcing. Eddies would separate the jets and dissipate the velocity of the slope jet. One implication of a slope jet is that it generates a flow in the opposite direction, in other words, a reversal below it. The reversed alongshore flow is reduced near the seafloor and consequently, generates an onshore flow in the bottom boundary layer.

[26] The development of the slope jet is controversial, although a few observations exist to support it along the slope of the Mid-Atlantic Bight. *Fratantoni and Pickart* [2003] deployed a moored array of ADCPs for 1 to 2 years to assess the mean flow of the shelf break jet. Their study found velocities of 0.1 m s^{-1} on the slope at 500 m depth. *Joyce et al.* [2005] also observed an equatorward jet on the slope 50–200 km offshore extending down to 4000 m in their data set collected over 10 years. *Flagg et al.* [2006] observed the slope jet in a subset of their ADCP data set, which was collected from a commercial ship on weekly

Figure 5. Time-averaged circulation for the summer case forced with an oscillating wind of period 10 days. Contours represent averaged density. Figures 5a, 5c, and 5e are averaged over periods of down-front wind stress (from the north), while Figures 5b, 5d, and 5f are averaged over periods of up-front wind stress (from the south). (a and b) The alongshore *u* velocity in m s^{-1}. (c and d) The cross-shelf *v* velocity in m s^{-1}. (e and f) The vertical velocity in mm s^{-1}. Positive velocities are down front, offshore, and up, for *u*, *v*, and *w* velocities, respectively. The color bars are not linear.
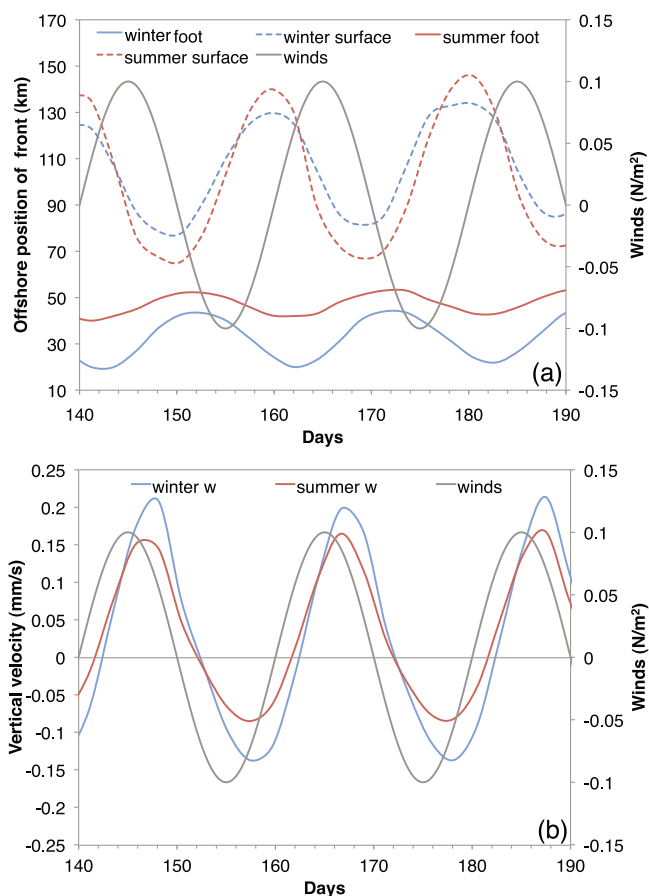
Figure 7. Results from the model forced by winds that oscillate between the up front and down front with a 10 day period. Winter is plotted in blue, and summer is plotted in red. (a) Mean offshore position of the foot and surface expression of the front from the model plotted along with the wind forcing over time. The lag between the maximal cross-shore migration of the front and the maximal wind forcing is about 5 days, which is equivalent to the Ekman spin-up time. (b) Mean vertical velocity averaged over the outer shelf bottom boundary layer plotted alongside wind forcing over time. The vertical velocity in the bottom boundary layer is proportional to the divergence in this layer.

transects between New Jersey and Bermuda over the course of 10 years. The slope jet was separated distinctly from the shelf break jet by an area of relatively low-velocity water, and velocities of 0.1 m s^{-1} were found down to 500 m depth in the observations of *Flagg et al.* [2006]; but the finding remains controversial owing to the elimination of some of the data. While contradictory data exist for the direction of the flow on the slope [*Fratantoni and Pickart*, 2007], results of the model agree with the observations of *Fratantoni and Pickart* [2003], *Joyce et al.* [2005] and *Flagg et al.* [2006] presented above.

[27] We were unable to eliminate the development of the slope jet in our model without resorting to restoring, so we quantify its contribution to tracer fluxes by comparing the spun-up solution with results from the time period prior to formation of the slope jet in the model. The presence of the slope jet increases the overall magnitude of the tracer fluxes

by a factor of two, but the mechanism for cross-frontal exchange of tracers remains robust both in the presence and absence of the slope jet.

[28] Our simulation differs from the real world in the behavior of the alongshore jet on the inner shelf, which usually flows toward the south in the real world, but in the model, is responds to the direction of the wind. The alternating alongshore flow in the model is caused by an alternation in the slope of the isopycnals near the coast between sloping upward and downward with the oscillating wind forcing. While upward tilted isopycnals are regularly observed on the inner shelf of the real ocean, the mean southward flow is usually merely weakened, and not reversed [*Whitney and Garvine*, 2005]. In our model, the inner shelf jet reverses more often than observed when forced with realistic winds.

[29] *Lentz* [2008] suggests that a large-scale barotropic pressure gradient maintains a southward flow on the inner shelf. Our experiments with imposed pressure gradient forcing did not result in a more realistic mean circulation than what we obtained without it, the results of which we present here. An offshore lateral density gradient observed on the inner shelf [*Whitney and Garvine*, 2005] suggests a source of fresh water at the coast, which is not included in the model and would result in a southward shelf flow. In general, the mechanism for maintaining the mean southward flow on the inner shelf remains unclear, and the remainder of the paper will focus on the outer shelf exchange.

[30] The foot of the front, defined as the grounding of the sigma 27 isopycnal, ranges between 60 m and 160 m depth, slightly deeper than observed. As shown in Figure 7, the foot of the front migrates offshore and deeper in response to northerly winds and shoals in response to southerly winds. The position of the front lags the wind forcing by about 5 days in the winter and 3 days in the summer, which is consistent with Ekman spin-up time calculated after *Greenspan* [1990] as:

$$T_c = E_z^{-\frac{1}{2}} f^{-1}, \quad where \quad E_z = \frac{K_z}{fd^2}, \qquad (6)$$

where f is the Coriolis parameter and E_z is the nondimensional Ekman number. Here K_z is the vertical viscosity and d is the depth of the mixed layer. In the winter, K_z has an average value of 0.001 m^2 s^{-1} and d extends to the full depth of the shelf (200 m), but in the summer, K_z has an average value of 0.0001 m^2 s^{-1} and d is 20 m or less, which results in a T_c of 5 days in the winter and 3 days in the summer.

[31] The cross-shelf velocities from the model are within the range of observations [*Flagg et al.*, 2006; *Biscaye et al.*, 1994] and are strongest in the surface and bottom Ekman layers, as seen in Figures 4e, 4f, 5c, and 5d and in Table 1. The time-averaged vertical velocities at the shelf break are well above 10 m d^{-1}, consistent with those suggested by *Houghton* [1997]. The vertical velocities range between −0.3 to 0.4 mm s^{-1} (−25 to 35 m d^{-1}) during southerly or up-front wind forcing and −0.3 to 0.6 mm s^{-1} (−25 to 52 m d^{-1}) during northerly or down-front wind forcing.

[32] Figure 8 depicts the modeled mean secondary circulation in response to southerly and northerly winds. The alternation between these states results in the onwelling and upwelling of nutrients, forming an efficient mechanism for
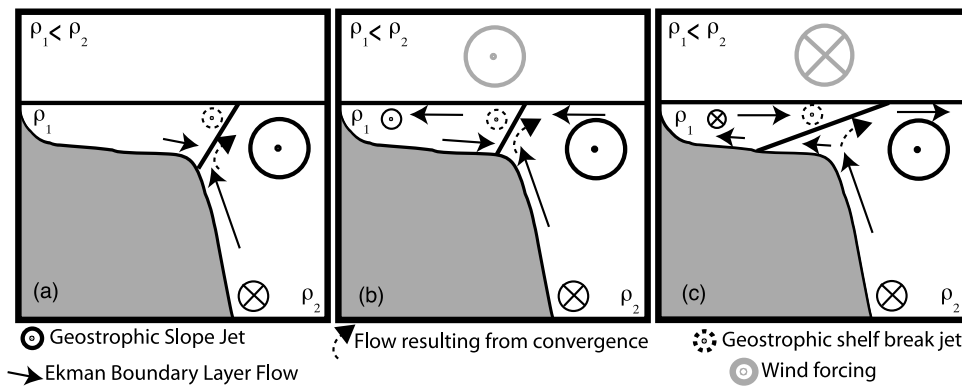
Figure 8. A depiction of the secondary circulation response to different wind forcings in the model: (a) no wind forcing, (b) down-front winds, and (c) up-front winds. Alternation between Figures 8b and 8c results in the continental shelf pump mechanism, whereby nutrients onwelled during the southerly wind phase are brought to the euphotic zone during the northerly wind phase. Arrows and symbols are not to scale.

nutrient supply to the euphotic zone. Northerly (down-welling) winds cause the isopycnals at the front to be nearly vertical. When winds reverse to southerly, the front leans offshore, with its foot moving shoreward.

[33] The tilt of the front is also affected by stratification of the water column, which impedes the migration of the foot of the front in the summertime [*Ou and Chen*, 2006]. The vertical velocity in the bottom boundary layer around the front is plotted with the wind forcing in Figure 7b, and can be used as a metric for convergence in the bottom boundary layer. There is more variation in winter because the dynamics of the front are unimpeded by the stratification on the shelf. However, in either season, onwelled slope water cannot reach the surface until the winds reverse directions, and an oscillation between up- and down-front winds is required to effectively pump water from the seafloor and the ocean interior to the ocean surface.

4.2. Tracer Results

[34] The behavior of the geochemical tracers depends on fluctuations in the wind (see Figures 9 and 10). Biological production of phytoplankton is fueled by upwelling nutrients from below, and so can be used as an index of the nutrient flux. Production is presented as a deviation from a 100 day climatological average from the model. Methane fluxes are presented as the efficiency with which methane released in the benthic boundary layer reaches the atmosphere, escaping chemical oxidation.

[35] Figures 9 and 10 depict the tracer flux results over time from the oscillating wind scenario with a 10 day period and from the realistic wind scenario, respectively. The variability in tracer fluxes is not in phase with the variability in winds. The lag between the change in wind direction and tracer response is due to the Ekman spin-up time and the time scale associated with the tracers, which is 6 days for nutrient uptake and 2 days for degassing.

[36] Biological production around the front decreases during southerly/up-front wind events, as shown in Figures 9b and 10b, despite the fact that nutrient-rich slope waters are actively supplied to the shelf during these events. The fraction of bottom boundary layer tracer from the slope increases in response to southerly winds, as shown in

Figures 9c and 10c, which indicates that slope water is supplied to the shelf. In Figure 10b, the biological production increases during a particularly long southerly wind event in the realistic wind record that induces traditional upwelling at the coast, and not around the front. As previously discussed, the traditional upwelling at the coast occurs in the model to a greater extent than in observations due to a weaker than observed alongshore flow near the coast. However, that mechanism is not the focus of this paper.

[37] Northerly wind events result in enhanced offshore flow in the bottom boundary layer and convergence at the front. Biological production around the front increases by 50–100% during these events, for example, there is a northerly wind event in the winter real-winds simulation in Figure 11b, in which biological production during a northerly wind event in the winter is seen to increase around the isopycnals of the front. From the surface view in Figure 11d, production is high around the front on the shelf side.

[38] The response of the methane tracer to the winds and bottom boundary layer convergence is consistent with the nutrient tracer as seen in Figures 9–12. The degassing flux of methane increases in response to both southerly and northerly wind forcing. In response to the southerly wind forcing, the traditional upwelling circulation brings deep methane-rich slope waters to the continental shelf. That water remains on the shelf for a while after the winds reverse and can be readily brought to the surface around the front to increase the flux by 10–200% during an episode of northerly wind. During the large events in the realistic wind-forcing case, methane is degassed at a higher rate than is released from the sediments, because the methane is building in the bottom boundary layer during the 20 days prior to the event when no northerly wind forcing occurred. In the model, methane follows the isopycnals to the surface. A plume of methane is seen in the cross section in Figure 11a extending upward from the bottom boundary layer along the isopycnals of the front and reaching the surface in places. The degassing flux is highest on the slope side of the front where the plume is larger.

[39] The length of time the winds blow from the north significantly increases the biological productivity. This can be seen in Figure 12, where the time-averaged production
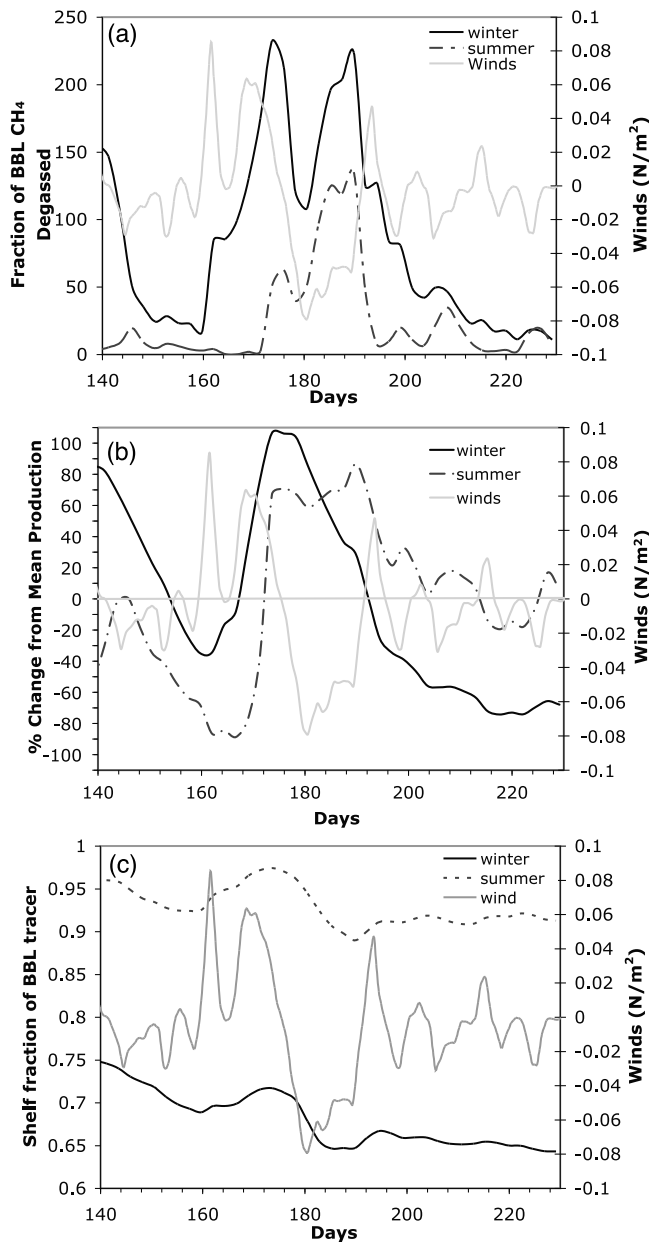
and the period is positively correlated ($R^2 = 0.96$) with the flux. The magnitude of the wind stress is also correlated with the degassing flux of methane ($R^2 = 0.93$). Stronger wind results in an increased degassing flux of methane and as shown in Figure 12b.

[40] In the summer cases, the response to the winds is different than in winter; biological production decreases in response to northerly winds. While high biological production can still be found around the front, the biological production is higher during southerly wind events than in response to northerly winds. In addition, as Figure 12c shows, biological production within the frontal region increases with
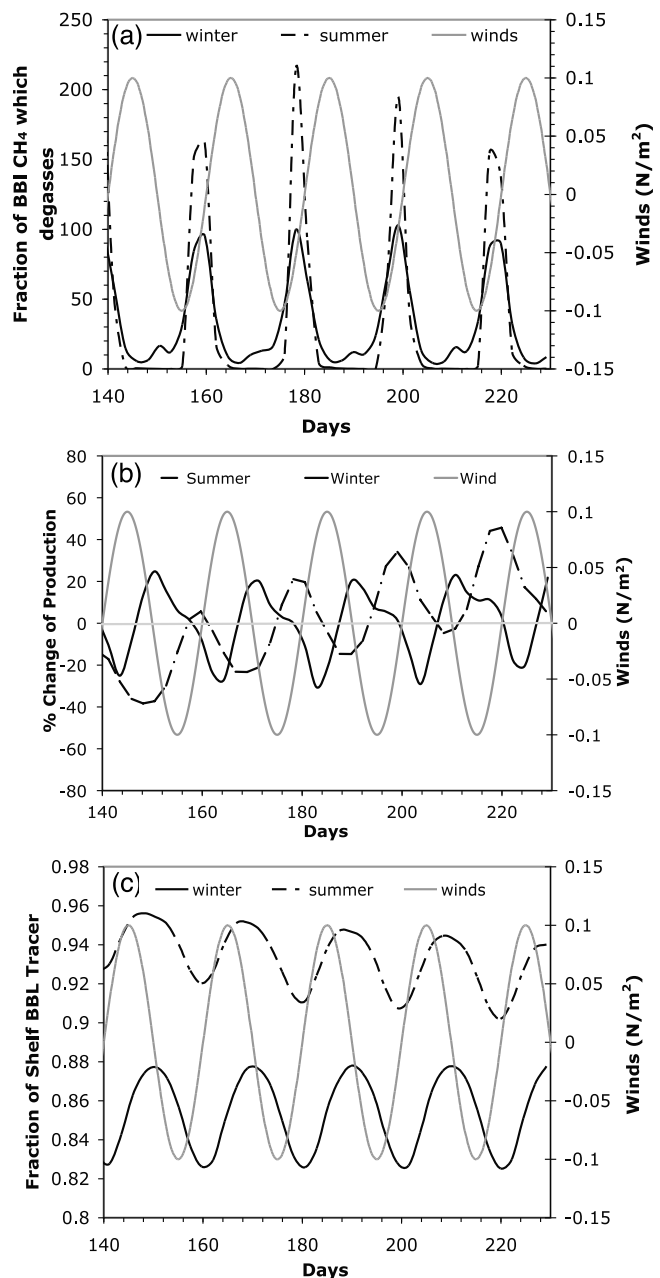
Figure 9. Tracer fluxes from the model: (a) ratio of the methane degassing rate to the rate of release from sediments, (b) percent change from mean biological production, and (c) fraction of total bottom boundary layer tracer that originated on the shelf, integrated over the shelf region. The model was forced with a realistic wind stress, as shown by the gray line. The summer simulation is plotted with the dashed line, while the winter is plotted with the solid black line.

for the modeled region is plotted against the period of the oscillating winds and they are significantly correlated ($R^2 = 0.85$). Longer periods of consistent wind direction result in higher production. The strength of the winds is also correlated to the production ($R^2 = 0.99$); stronger winds result in higher biological production. Longer periods of consistent wind direction, both northerly and southerly, result in increased degassing of methane, as shown in Figure 12a,

Figure 10. Same as Figure 9 but the model was forced by an idealized oscillating wind with a period of 10 days, as shown by the gray line.
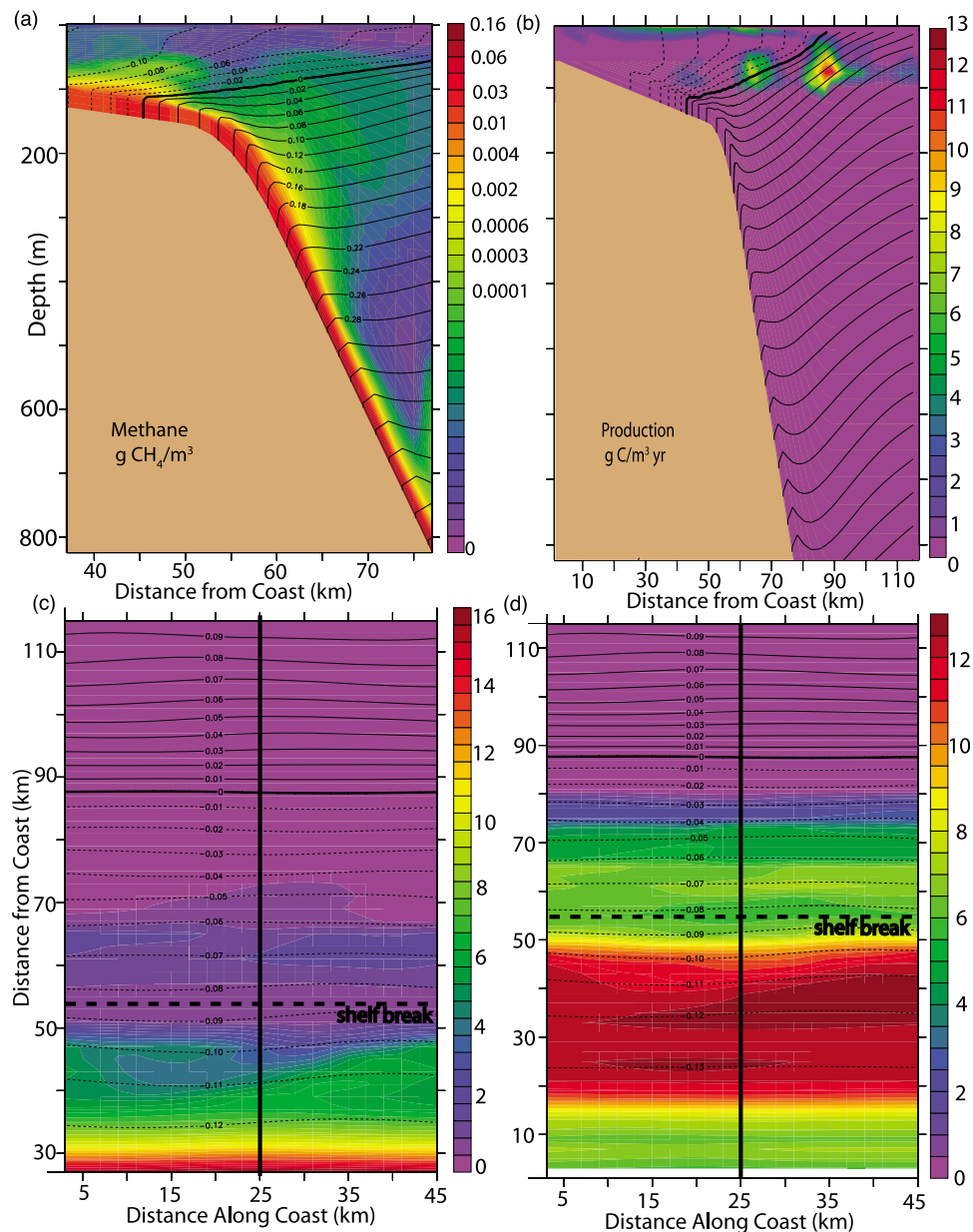
Figure 11. Tracer fluxes from a winter simulation forced with an oscillating wind. Surface and cross-sectional views are shown on day 190, where the wind is nearly at its maximum down-front strength. (a) Cross-sectional view of methane concentration on a logarithmic color scale with density contours in black. The cross section is taken from the location marked in Figure 11c. (b) Cross-sectional view of biological production converted from nitrogen using a constant Redfield ratio with density contours in black. (c) Surface view for the degassing of methane in g CH_4 m^{-2} yr^{-1} with density contours in black. (d) Surface cross section for biological production in g C m^{-2} yr^{-1} with density contours in black. The location of the shelf break and the cross section are marked in Figures 11c and 11d.

increased stratification. With stratification, the movement of the foot of the front is restricted. Consequently, nutrients are upwelled at the shelf break in the summer instead of onwelled onto the shelf, as in the winter case. The summer-time degassing flux of methane also decreases in response to northerly winds.

[41] Figure 8 simplifies the mechanism for transporting nutrients into a two-dimensional cartoon, in which the role of alongshore variations (i.e., frontal meandering and eddies) is neglected. The front is inherently unstable due to bar-oclinic instability, but the variability that develops in our model is smaller than we expect in reality due to the uniform alongshore forcing in the model. We find that it is the along-shore mean flow and secondary circulation, rather than the eddy fluxes, that determines the nutrient fluxes. Experiments in which we varied the along-shore size of domain from just
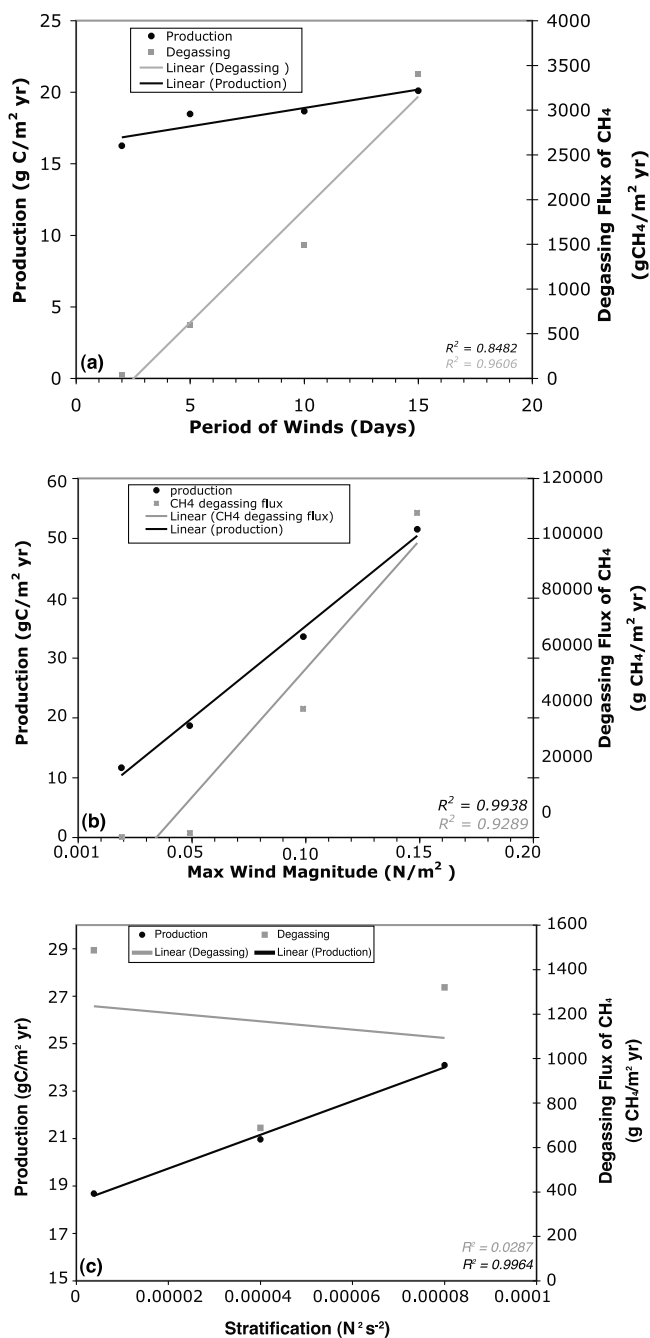
Figure 12. Comparisons of the tracer fluxes to wind and density forcing. (a) Biological production and degassing of methane plotted against the period of the winds show the results of varying the period of the oscillation from 2 to 15 days. Both tracer fluxes increase with longer periods. (b) Biological production and degassing of methane plotted against the amplitude of the oscillatory wind stress with a period of 10 days. Both tracer fluxes increase with increased wind magnitude. (c) Biological production and degassing of methane plotted against varying strengths of stratification. Biological production increases with increasing stratification, while degassing of methane has no relationship with stratification.

16 km to a few hundred km resulted in the conclusion that the mean circulation determines the tracer, creating an essentially two-dimensional scenario for the fluxes. It is possible that this is because the model simplifies or neglects various aspects of the coastal setting which may influence this result. For example, the alongshore bathymetry is constant, the influence of Gulf Stream rings is neglected, tides, cross-shelf winds, and alongshore variability in wind stress are not considered. Experiments with more realistic forcing and eddy variability would be necessary to quantify the role of eddies in transporting nutrients in the real coastal ocean.

4.3. Implications of the Shelf Break Pump Mechanism

[42] We estimate the global impact of geochemical ventilation at the shelf break front by averaging the vertical velocities in the model in a 10 km band over the shelf break and extrapolating their effects to other shelf break fronts around the globe. The average vertical velocity for the summer case with down-front winds is 13 m d^{-1} and for the winter case with down-front winds is 17 m d^{-1}. Applying these velocities to other areas around the world characterized by a similar frontal system, depicted in Figure 1, we compute annually averaged volume flux of ventilating upwelling of about 16 Sv. If that water is rich in nutrients and gases as in the Mid-Atlantic Bight, the fluxes could be significant in global biogeochemical calculations.

[43] The shelf break pump mechanism modulates the flux of nutrient into the euphotic zone by about a factor of two, between northerly and southerly wind forcing. Assuming then that the pump is responsible for about half of the roughly 300 g C m^{-2} yr^{-1} coastal biological production rate. Over the northeast coast of the Unites States, assuming 2000 km of coastline and a 10 km wide band of influence along the shelf break region, the shelf break pump mechanism could supply 0.5–1 Tg N yr^{-1}, about three times the total nitrogen delivered to that shelf from estuaries, which is estimated as 0.18–0.36 Tg N yr^{-1} [*Nixon et al.*, 1996]. Assuming that the other areas in the world dominated by a similar frontal system outlined in red in Figure 1 have consistent nutrient supply, and that the area of the red regions in Figure 1 is about 90,000 km^2, then the nutrient supplied to the coastal ocean by this mechanism is 2.5–5 Tg N yr^{-1}; that is, about 10–20% of the global total nitrogen flux from rivers, which is estimated to be 25 Tg N yr^{-1} [*Wollast*, 1991].

[44] The global source of methane from coastal sediments to the benthic boundary layer has been estimated to be between 8 and 65 Tg CH$_4$ annually [*Hovland et al.*, 1993]. If 20% were to escape via the shelf break pump, that would result in a global flux of methane from the coastal ocean of 1.6–13 Tg CH$_4$ annually, or 0.3–3% of the global source of methane to the atmosphere of 500 Tg CH$_4$ yr^{-1} [*Reeburgh*, 2007].

5. Conclusion

[45] From process studies performed with a high-resolution ocean model for the Mid-Atlantic Bight, we propose a new mechanism for nutrient supply and ventilation of benthic gases in the coastal ocean. Wind direction alters both the position and the slope of the isopycnals of the front, which become more vertical in response to northerly (down front)

winds and flatten in response to southerly (up front) winds. Both degassing of methane, and biological production, increase in response to northerly winds during the winter. Southerly winds pump water from the bottom boundary layer of the slope onto the outer shelf and trap the nutrients and gases under the flattened front.

[46] The oscillation between northerly and southerly winds pumps water from the bottom boundary layer up to the surface. The longer the winds blow from the south, the more nutrients and gases build under the front. When the winds shift direction to northerly, the nutrients and gases that had been building in the bottom boundary layer escape to the surface, which results in increased biological production and degassing of methane to the atmosphere. Thermal stratification of the waters on the shelf during summer restricts the operation of the shelf break pump mechanism because it inhibits the movement of the foot of the front.

[47] It is computationally challenging to simulate the impact of the coastal carbon cycle on the geochemistry of the ocean, but it is clear that the impacts of processes such as the shelf break pump can be significant on a global scale.

Appendix A

[48] The dimensionless equations that comprise this non-hydrostatic free-surface model are written as:

$$\frac{Du}{Dt} + \frac{1}{\varepsilon}(gh_x + r_x + \delta q_x - fv + \varepsilon \delta bw) = \partial_z(K_z u_z) \tag{A1}$$

$$\frac{Dv}{Dt} + \frac{1}{\varepsilon}(gh_y + r_y + \delta q_y + fu) = \partial_z(K_z v_z) \tag{A2}$$

$$\frac{Dw}{Dt} + \alpha(q_z - bu) = 0 \tag{A3}$$

$$u_x + v_y + \varepsilon w_z = 0 \tag{A4}$$

$$\frac{\partial h}{\partial t} + \frac{\varepsilon}{F_r^2}\left(\partial_x\left(\int_{-d}^{\frac{H}{D}h} u \, dz\right) + \partial_y\left(\int_{-d}^{\frac{H}{D}h} v \, dz\right)\right) = 0 \tag{A5}$$

where

$$\frac{D}{Dt} \equiv \frac{\partial}{\partial t} + u\frac{\partial}{\partial x} + v\frac{\partial}{\partial y} + \varepsilon w\frac{\partial}{\partial z}$$

The northward and eastward distances are defined by x and y, respectively, while z is the vertical coordinate, and t is time. The velocities u, v, w are in the x, y, z directions, respectively. The Rossby number is denoted by ε and is equivalent to U/fL, where U is the characteristic velocity, f is the Coriolis parameter, and L is the horizontal length scale. The Coriolis parameters are $f = 2\Omega\sin(\phi) = 5 \times 10^{-5}$ s^{-1} and $b = 2\Omega\cos(\phi) = 1 \times 10^{-4}$ s^{-1} where ϕ is the latitude. The aspect ratio of the depth scale D to length scale L is represented by δ in equations (A1) and (A2). The vari-

able ρ represents potential density, h the elevation of the free surface, q the nonhydrostatic component of the pressure, r the hydrostatic pressure due to the density variations from the mean, a the distance from the center of the Earth, d is the mixed layer depth, H/D is the ratio of the characteristic free surface elevation to depth scale. The value of the coefficient α is $1/\varepsilon^2\delta$. All variables have been nondimensionalized.

[49] The winds also influence the flow through the surface boundary condition:

$$K_z \frac{du}{dz} = \frac{-\tau}{\rho} \tag{A6}$$

where K_z is the vertical viscosity determined from the shear and the buoyancy frequency by the General Ocean Turbulence Model (GOTM) using the Mellor-Yamada 2.5 turbulence closure scheme [*Mellor and Yamada*, 1982], but restricted to a maximum value of 0.001 m^2 s^{-1}. Wind stresses in the x and y direction are represented by τ_x and τ_y.

[50] The boundary conditions for GOTM were modified to fit our model, and parameters used in GOTM are determined by equations (A7)–(A10). In GOTM, we specify the following parameters:

$$z_0^s = \frac{0.4}{f}\sqrt{\frac{\tau}{\rho_0}} \tag{A7}$$

where ρ_0 is the reference density of 1025 kg m^{-3} and z_0^s is the surface roughness parameter. The boundary conditions at the bottom are:

$$u_*^b = r_r\left[U_{bottom}^2 + V_{bottom}^2\right] \tag{A8}$$

$$z_0^b = 0.4\frac{u_*^b}{f} \tag{A9}$$

$$K_z u_z = r_r u \tag{A10}$$

where r_r is a bottom friction, which has a constant value of 0.0005 m s^{-1} u_*^b is the frictional velocity on the bottom, and z_0^b is the bottom roughness parameter.

[51] An idealized topography is implemented using an empirical relationship after *Gawarkiewicz and Chapman* [1992]:

$$\eta(y) = \begin{cases} 50. + 2y & \text{for} & y < 50 \\ 160. + 1.5(y-50)^2 - 0.1(y-60)^2 & \text{for} & 50 < y < 60 \\ 310. + 30.(y-60) & \text{for} & 60 < y < 80 \\ 1060. - 1.5(y-90)^2 & \text{for} & 80 < y < 90 \\ 1060. & \text{for} & y > 90 \end{cases} \tag{A11}$$

where η is depth in m and y is the offshore distance in km.

References

Aikman, F., H. W. Ou, and R. W. Houghton (1988), Current variability across the New England continental shelf-break and slope, *Cont. Shelf Res.*, 8, 625–651, doi:10.1016/0278-4343(88)90069-6.

Atkinson, L. P., P. G. O'Malley, J. A. Yoder, and G. A. Paffenhofer (1984), The effect of summertime shelf break upwelling on nutrient flux in southeastern United States continental shelf waters, *J. Mar. Res.*, 42, 969–993, doi:10.1357/002224084788520756.

Biscaye, P. E., C. N. Flagg, and P. G. Falkowski (1994), The Shelf Edge Exchange Processes experiment (SEEP-II): An introduction to hypotheses, results and conclusions, *Deep Sea Res. Part II*, 41, 231–252, doi:10.1016/0967-0645(94)90022-1.

Campos, E. J. D., D. Velhote, and I. C. A. da Silveira (2000), Shelf break upwelling driven by Brazil Current cyclonic meanders, *Geophys. Res. Lett.*, 27, 751–754, doi:10.1029/1999GL010502.

Castelao, R. M., E. J. D. Campos, and J. L. Miller (2004), A modelling study of coastal upwelling driven by wind and meanders of the Brazil current, *J. Coastal Res.*, 203, 662–671, doi:10.2112/1551-5036(2004)20[662:AMSOCU]2.0.CO;2.

Chapman, D. C. (2000), Boundary layer control of buoyant coastal currents and the establishment of a shelfbreak front, *J. Phys. Oceanogr.*, 30, 2941–2955, doi:10.1175/1520-0485(2001)031<2941:BLCOBC>2.0.CO;2.

Chapman, D. C., and S. J. Lentz (1994), Trapping of a coastal density front by the bottom boundary-layer, *J. Phys. Oceanogr.*, 24, 1464–1479, doi:10.1175/1520-0485(1994)024<1464:TOACDF>2.0.CO;2.

DeGrandpre, M. D., G. J. Olbu, C. M. Beatty, and T. R. Hammar (2002), Air-sea CO₂ fluxes on the U.S. Middle Atlantic Bight, *Deep Sea Res. Part II*, 49, 4355–4367, doi:10.1016/S0967-0645(02)00122-4.

Elskens, M., W. Baeyens, and L. Goeyens (1997), Contribution of nitrate to the uptake of nitrogen by phytoplankton in an ocean margin environment, *Hydrobiologia*, 353, 139–152, doi:10.1023/A:1003058928157.

Flagg, C. N., M. Dunn, D.-P. Wang, H. T. Rossby, and R. L. Benway (2006), A study of the currents of the outer shelf and upper slope from a decade of shipboard ADCP observations in the Middle Atlantic Bight, *J. Geophys. Res.*, 111, C06003, doi:10.1029/2005JC003116.

Fratantoni, P. S., and R. S. Pickart (2003), Variability of the shelf break jet in the Middle Atlantic Bight: Internally or externally forced?, *J. Geophys. Res.*, 108(C5), 3166, doi:10.1029/2002JC001326.

Fratantoni, P. S., and R. S. Pickart (2007), The western North Atlantic shelfbreak current system in summer, *J. Phys. Oceanogr.*, 37, 2509–2533, doi:10.1175/JPO3123.1.

Gawarkiewicz, G., and D. C. Chapman (1992), The role of stratification in the formation and maintenance of shelf-break fronts, *J. Phys. Oceanogr.*, 22, 753–772, doi:10.1175/1520-0485(1992)022<0753:TROSIT>2.0.CO;2.

Greenspan, H. P. (1990), *The Theory of Rotating Fluids*, Breukelen, Brookline, Mass.

Hales, B., R. D. Vaillancourt, L. Prieto, J. Marra, R. Houghton, and D. Hebert (2009a), High-resolution surveys of the biogeochemistry of the New England shelfbreak front during Summer, 2002, *J. Mar. Syst.*, 78, 426–441, doi:10.1016/j.jmarsys.2008.11.024.

Hales, B., D. Hebert, and J. Marra (2009b), Turbulent supply of nutrients to phytoplankton at the New England shelf break front, *J. Geophys. Res.*, 114, C05010, doi:10.1029/2008JC005011.

Harrison, W. G., L. R. Harris, and B. D. Irwin (1996), The kinetics of nitrogen utilization in the oceanic mixed layer: Nitrate and ammonium interactions at nanomolar concentrations, *Limnol. Oceanogr.*, 41, 16–32, doi:10.4319/lo.1996.41.1.0016.

Hill, A. E., B. M. Hickey, F. A. Shillington, P. T. Strub, K. H. Brink, E. D. Barton, and A. C. Thomas (1998), Eastern ocean boundaries, in *The Sea*, vol. 11, edited by A. R. Robinson and K. H. Brink, pp. 29–67, John Wiley, New York.

Houghton, R. W. (1997), Lagrangian flow at the foot of a shelfbreak front using a dye tracer injected into the bottom boundary layer, *Geophys. Res. Lett.*, 24, 2035–2038, doi:10.1029/97GL02000.

Houghton, R. W., and M. Visbeck (1998), Upwelling and convergence in the Middle Atlantic Bight shelfbreak front, *Geophys. Res. Lett.*, 25, 2765–2768, doi:10.1029/98GL02105.

Hovland, M., A. G. Judd, and R. A. Burke (1993), The global flux of methane from shallow submarine sediments, *Chemosphere*, 26, 559–578, doi:10.1016/0045-6535(93)90442-8.

Joyce, T. M., J. Dunworth-Baker, R. S. Pickart, D. Torres, and S. Waterman (2005), On the deep western boundary current south of Cape Cod, *Deep Sea Res. Part II*, 52, 615–625, doi:10.1016/j.dsr2.2004.12.013.

Lathuilière, C., V. Echevin, M. Lévy, and G. Madec (2010), On the role of the mesoscale circulation on an idealized coastal upwelling ecosystem, *J. Geophys. Res.*, 115, C09018, doi:10.1029/2009JC005827.

Lentz, S. J. (2008), Observations and a model of the mean circulation over the Middle Atlantic Bight continental shelf, *J. Phys. Oceanogr.*, 38, 1203–1221, doi:10.1175/2007JPO3768.1.

Linder, C. A., and G. Gawarkiewicz (1998), A climatology of the shelf-break front in the Middle Atlantic Bight, *J. Geophys. Res.*, 103, 18,405–18,423, doi:10.1029/98JC01438.

Linder, C. A., G. G. Gawarkiewicz, and R. S. Pickart (2004), Seasonal characteristics of bottom boundary layer detachment at the shelfbreak front in the Middle Atlantic Bight, *J. Geophys. Res.*, 109, C03049, doi:10.1029/2003JC002032.

Loder, J. W., W. C. Boicourt, and J. H. Simpson (1998a), Western ocean boundary shelves: Coastal segment (W), in *The Sea*, vol. 11, edited by A. R. Robinson and K. H. Brink, pp. 3–27, John Wiley, New York.

Loder, J. W., B. Petrie, and G. Gawarkiewicz (1998b), The coastal ocean off northeastern North America: A large-scale view, in *The Sea*, vol. 11, edited by A. R. Robinson and K. H. Brink, pp. 105–133, John Wiley, New York.

Lozier, M. S., and G. Gawarkiewicz (2001), Cross-frontal exchange in the Middle Atlantic Bight as evidenced by surface drifters, *J. Phys. Oceanogr.*, 31, 2498–2510, doi:10.1175/1520-0485(2001)031<2498:CFEITM>2.0.CO;2.

Mahadevan, A. (2006), Modeling vertical motion at ocean fronts: Are nonhydrostatic effects relevant at submesoscales?, *Ocean Modell.*, 14, 222–240, doi:10.1016/j.ocemod.2006.05.005.

Mahadevan, A., and D. Archer (2000), Modeling the impact of fronts and mesoscale circulation on the nutrient supply and biogeochemistry of the upper ocean, *J. Geophys. Res.*, 105, 1209–1225, doi:10.1029/1999JC900216.

Mahadevan, A., J. Oliger, and R. A. Street (1996a), A nonhydrostatic mesoscale ocean model. Part 1. Well-posedness and scaling, *J. Phys. Oceanogr.*, 26, 1868–1880, doi:10.1175/1520-0485(1996)026<1868:ANMOMP>2.0.CO;2.

Mahadevan, A., J. Oliger, and R. A. Street (1996b), A nonhydrostatic mesoscale ocean model. Part 2. Numerical implementation, *J. Phys. Oceanogr.*, 26, 1881–1900, doi:10.1175/1520-0485(1996)026<1881:ANMOMP>2.0.CO;2.

Mellor, G. L., and T. Yamada (1982), Development of a turbulence closure-model for geophysical fluid problems, *Rev. Geophys.*, 20, 851–875, doi:10.1029/RG020i004p00851.

Mizobata, K., J. Wang, and S. Saitoh (2006), Eddy-induced cross-slope exchange maintaining summer high productivity of the Bering Sea shelf break, *J. Geophys. Res.*, 111, C10017, doi:10.1029/2005JC003335.

Newman, K. R., et al. (2008), Active methane venting observed at giant pockmarks along the US mid-Atlantic shelf break, *Earth Planet. Sci. Lett.*, 267, 341–352, doi:10.1016/j.epsl.2007.11.053.

Nixon, S. W., et al. (1996), The fate of nitrogen and phosphorus at the land sea margin of the North Atlantic Ocean, *Biogeochemistry*, 35, 141–180, doi:10.1007/BF02179826.

Okkonen, S. R., T. J. Weingartner, S. L. Danielson, D. L. Musgrave, and G. M. Schmidt (2003), Satellite and hydrographic observations of eddy-induced shelf-slope exchange in the northwestern Gulf of Alaska, *J. Geophys. Res.*, 108(C2), 3033, doi:10.1029/2002JC001342.

Ou, H. W., and D. Chen (2006), Wind-induced shear dispersion and genesis of the shelf-break front, *Prog. Oceanogr.*, 70, 313–330, doi:10.1016/j.pocean.2006.03.015.

Pelegrí, J. L., and G. T. Csanady (1991), Nutrient transport and mixing in the Gulf Stream, *J. Geophys. Res.*, 96, 2577–2583, doi:10.1029/90JC02535.

Pickart, R. S. (2000), Bottom boundary layer structure and detachment in the shelfbreak jet of the Middle Atlantic Bight, *J. Phys. Oceanogr.*, 30, 2668–2686, doi:10.1175/1520-0485(2001)031<2668:BBLSAD>2.0.CO;2.

Rasmussen, L. L., G. Gawarkiewicz, W. B. Owens, and M. S. Lozier (2005), Slope water, Gulf Stream, and seasonal influences on southern Mid-Atlantic Bight circulation during the fall-winter transition, *J. Geophys. Res.*, 110, C02009, doi:10.1029/2004JC002311.

Reeburgh, W. S. (2007), Oceanic methane biogeochemistry, *Chem. Rev.*, 107, 486–513, doi:10.1021/cr050362v.

Ryan, J. P., J. A. Yoder, J. A. Barth, and P. C. Cornillon (1999), Chlorophyll enhancement and mixing associated with meanders of the shelf break front in the Mid-Atlantic Bight, *J. Geophys. Res.*, 104, 23,479–23,493, doi:10.1029/1999JC900174.

Shaw, P. T., L. J. Pietrafesa, C. N. Flagg, R. W. Houghton, and K. H. Su (1994), Low-frequency oscillations on the outer shelf in the southern Mid-Atlantic Bight, *Deep Sea Res. Part II*, 41, 253–271, doi:10.1016/0967-0645(94)90023-X.

Valentine, D. L., D. C. Blanton, W. S. Reeburgh, and M. Kastner (2001), Water column methane oxidation adjacent to an area of active hydrate

dissociation, Eel River Basin, *Geochim. Cosmochim. Acta*, *65*, 2633–2640, doi:10.1016/S0016-7037(01)00625-1.

Walsh, J. J., P. E. Biscaye, and G. T. Csanady (1988), The 1983–1984 Shelf Edge Exchange Processes (SEEP-I) experiment: Hypotheses and highlights, *Cont. Shelf Res.*, *8*, 435–456, doi:10.1016/0278-4343(88)90063-5.

Whitney, M. M., and R. W. Garvine (2005), Wind influence on a coastal buoyant outflow, *J. Geophys. Res.*, *110*, C03014, doi:10.1029/2003JC002261.

Wollast, R. (1991), The coastal organic carbon cycle: Fluxes, sources, and sinks, in *Ocean Margin Processes in Global Change*, edited by R. F. C. Mantoura, J. M. Martin, and R. Wollast, pp. 365–381, John Wiley, New York.

D. E. Archer and S. A. Siedlecki, Department of Geophysical Sciences, University of Chicago, 5734 S. Ellis Ave., Chicago, IL 60637, USA. (siedlesa@uchicago.edu)

A. Mahadevan, Department of Earth Sciences, Boston University, 675 Commonwealth Ave., Boston, MA 02215, USA.